Single-Chain Nanoparticles

Star-Like Aggregates

ROYAL SOCIETY
OF **CHEMISTRY**

PAPER
Magali Gary-Bobo, José A. Pomposo, Fabienne Dumoulin *et al.*
Topology effects in photodynamic therapy with
phthalocyanine nanocarriers

PAPER

Check for updates

Topology effects in photodynamic therapy with phthalocyanine nanocarriers†

Davide Arena,[a] Ümit İşci, [ID] [b] Mélanie Onofre,[c] Christophe Nguyen,[c] Zeynel Şahin, [ID] [b] Ester Verde-Sesto,[ad] Amaia Iturrospe,[a] Arantxa Arbe,[a] Magali Gary-Bobo, [ID] *[c] José A. Pomposo [ID] *[ade] and Fabienne Dumoulin [ID] *[f]

Two different amphiphilic copolymers, a random copolymer (**RCP**) and a block copolymer (**BCP**), have been used to encapsulate a far-red photosensitizing hydrophobic zinc phthalocyanine while forming self-assembled nanocarriers of different topology: self-folded single-chain nanoparticles (**SCNPs**) and star-like aggregates (**SLAs**), respectively. Different copolymer/phthalocyanine ratios have been tested to assess their effect on structural properties which were determined by small-angle X-ray scattering (SAXS) measurements. The relevance of these materials as photosensitizer nanocarriers for photodynamic therapy (PDT) has been studied against human breast cancer cells (MCF-7). A better PDT effect was found for the **SCNP-Pc2$_x$** (100 µg mL^{-1}) excited at 800 nm with a pulsed laser than for the **SLA-Pc2$_x$** under identical conditions. Conversely, irradiation at slightly lower wavelengths (740 nm) of MCF-7 cells incubated with **SLA-Pc2$_x$** resulted in a notorious PDT effect when compared to that observed for MCF-7 cells incubated with the **SCNP-Pc2$_x$**. These systems represent new strategies for the encapsulation of photosensitizers for photodynamic therapy.

1. Introduction

Photodynamic therapy (PDT) is now a well-recognized treatment of cancer, even though it is still too often described as emerging. The first photosensitizers were approved decades ago,[1,2] but had several drawbacks in terms of characterization, tumor targeting and efficiency. Second generation-photosensitizers have since been approved or are in advanced clinical trials.[3–5] Using excitation wavelengths belonging to the first phototherapeutic window (600–1000 nm) for PDT is advantageous for two reasons: first, it avoids exciting endogenous chromophores,[6] and second, it allows deeper light penetration into biological tissues than with shorter wavelengths.[7] Phthalocyanines are synthetic tetrapyrrolic molecules of the porphyrinoid family and show typically an average maximum absorption at 700 nm. In this respect, phthalocyanines are excellent photosensitizer molecular bases for anti-cancer PDT.[8–11] Many water-soluble phthalocyanines with cationic, anionic or neutral substituents have been used for PDT.[12] However, they are frequently aggregated, which impairs their efficiency. Besides, excessive water-solubility of photosensitizers may be detrimental since it induces a rapid clearance from the body without having the chance to accumulate in the targeted tissues, and/or prevents cellular internalization by limiting the cellular membrane crossing. The use of hydrophobic photosensitizers overcomes these issues, but a significant drawback is that they are not biocompatible as they cannot circulate in the bloodstream. This promoted the use of various nanocarriers, either by encapsulation or by covalent grafting of the hydrophobic photosensitizer.[13] An additional advantage is that nanoformulated photosensitizers can benefit from the enhanced permeability and retention (EPR) effect, which may have some limitations[14] but is anyway a good way to deliver photosensitizers. A liposomal formulation of unsubstituted zinc phthalocyanine has entered advanced clinical trials,[15] and several micellar formulations of phthalocyanine derivatives for PDT applications have been reported.[16,17] Conjugating a mono-hydroxylated phthalocyanine to poly-L-glutamic acid allowed to obtain polymeric nanoparticles of high efficiency,[18,19] and phthalocyanine-based organo-silica nanoparticles exhibited remarkable photodynamic

[a] Centro de Física de Materiales (CSIC, UPV/EHU) and Materials Physics Center MPC, Paseo Manuel Lardizabal 5, 20018 Donostia, Spain.
E-mail: josetxo.pomposo@ehu.eus

[b] Marmara University, Faculty of Technology, Department of Metallurgical and Materials Engineering, 34854 Maltepe, Istanbul, Türkiye

[c] Institut des Biomolécules Max Mousseron, CNRS, ENSCM, 34293 Montpellier, France. E-mail: magali.gary-bobo@inserm.fr

[d] IKERBASQUE–Basque Foundation for Science, Plaza de Euskadi 5, 48009 Bilbao, Spain

[e] Departamento de Polímeros y Materiales Avanzados, Física, Química y Tecnología, University of the Basque Country (UPV/EHU), 20800 Donostia, Spain

[f] Acıbadem Mehmet Ali Aydınlar University, Faculty of Engineering and Natural Sciences, Department of Biomedical Engineering, 34752 Ataşehir, Istanbul, Türkiye. E-mail: fabienne.dumoulin@acibadem.edu.tr

† Electronic supplementary information (ESI) available. See DOI: https://doi.org/10.1039/d4ma00524d

efficiency.[20,21] It has been shown that the nature of the polymeric nanocarrier can greatly affect the photodynamic efficiency of a nano-photosensitizing system.[22]

Self-assembled nanocarriers such as single-chain nanoparticles (**SCNPs**) have proven to be efficient carriers for the delivery of hydrophobic drugs.[23–25] These works are relatively recent. Indeed, only a handful of tetrapyrrolic derivatives combined with **SCNPs** have been reported: a porphyrin has been grafted onto the skeleton of individual **SCNPs**;[26] phthalonitriles (which are the most common precursor of phthalocyanines) have been introduced on a polystyrene backbone, the subsequent intramolecular formation of the phthalocyanine moiety leading to the formation of colored single-chain polymeric nanoparticles;[27] and the axial coordination of a polymeric chain containing pyridine moieties by a cobalt phthalocyanine produced CO_2-reducing materials.[28]

In this work, a photosensitizing far-red absorbing hydrophobic zinc phthalocyanine has been designed to be encapsulated into two different polymeric nanocarriers prepared from the same monomers. The random copolymer self-assembled into self-assembled single-chain nanoparticles (**SCNPs**), and the block copolymer formed star-like aggregates (**SLAs**). A careful characterization of the resulting phthalocyanine-loaded nanocarriers (**SCNP-Pc2$_x$** and **SLA-Pc2$_x$**) was carried out by means of small-angle X-ray scattering (SAXS) experiments. Finally, we report how the very different topology of these two nanocarriers modulate the PDT efficiency on MCF-7 breast cancer cells.

2. Experimental

2.1. Chemistry

2.1.1. Materials and methods. Oligo(ethyleneglycol)monomethylether methacrylate (OEGMA$_{300}$) (99%), (2-acetoacetoxy)-ethyl methacrylate (AEMA) (95%), 2,2′-azobis(2-methylpropionitrile) (AIBN) ($\geq$ 98%), 1,4-dioxane, n-hexane, deuterated chloroform (CDCl$_3$) (99.96 atom% D, containing 0.03% (v/v) tetramethylsilane, TMS), sodium phosphate dibasic heptahydrate (Na$_2$HPO$_4$· 7H$_2$O), sodium phosphate monobasic monohydrate (NaH$_2$PO$_4$· H$_2$O) were purchased from Sigma-Aldrich and used, unless specified, as received. 4-Cyanopentanoic acid dithiobenzoate (CPADB) ($\geq$ 97%) was purchased from Strem Chemicals. Methanol and tetrahydrofuran (THF) (HPLC grade) were purchased from Scharlab. AIBN was recrystallized from methanol. OEGMA$_{300}$ and AEMA were purified by passing through basic alumina. 3-Nitrophthalonitrile, isobutylthiol, hexadeuterated dimethylsulfoxide (DMSO-d_6), dimethylformamide (DMF), potassium carbonate (K$_2$CO$_3$), dimethyl sulfoxide (DMSO), zinc acetate Zn(OAc)$_2$, dimethylaminoethanol and dichloromethane were used as purchased. Column chromatographies were done using Merck Silica Gel 60 (0.040–0.063 mm). NMR spectra were recorded at room temperature in CDCl$_3$ or DMSO-d_6 solutions on a Varian spectrometer (500 MHz for ^{1}H, 125 MHz for ^{13}C spectra). FT-IR spectra were recorded between 4000 and 650 cm^{-1} using a PerkinElmer Spectrum 100 FT-IR spectrometer. Mass spectra were measured on a MALDI (matrix assisted laser desorption

ionization) BRUKER Microflex LT (Bremen, Germany) using 2,5-dihydroxybenzoic acid as the matrix.

2.1.2. Synthesis of 3-isobutylthiophthalonitrile (1). 3-Nitrophthalonitrile (5 g, 28.8 mmol), isobutylthiol (2.9 g, 33.2 mmol) and dry potassium carbonate (30 g, 217.5 mmol) were stirred in anhydrous DMF (50 mL) under argon at 40 °C for 24 h until complete disappearance of 3-nitrophthalonitrile in TLC monitoring. Then the reaction mixture was poured into water (500 mL), and the resulting solid was collected by filtration and thoroughly washed with water. The dried crude product was recrystallized from ethanol. Yield: 80% (4.98 g). ^{1}H NMR (500 MHz, CDCl$_3$) δ, ppm: 7.61–7.56 (m, 3 H), 2.96 (d, 2H), 1.96 (m, 1 H), 1.11 (d, 6 H). ^{13}C NMR (125 MHz, CDCl$_3$) δ, ppm: 146.3, 132.6, 131.1, 129.4, 117.2, 115.3, 114.7, 113.8, 41.9, 28.1, 21.9. FT-IR (ν, cm^{-1}): 3090, 2973, 2956, 2934, 2230, 1566, 1454, 1421, 1385, 1319, 1259, 1198, 1153, 1083, 958, 792, 726.

2.1.3. Synthesis of phthalocyanine Pc2. A mixture of **1** (1 g, 4.62 mmol) and Zn(OAc)$_2$ (424 mg, 2.31 mmol) was refluxed in dimethylaminoethanol (10 mL) under argon for 12 h. After cooling to room temperature, the reaction mixture was poured into water (100 mL). The resulting precipitate was filtered off and washed several times with ethanol. **Pc2** was isolated by chromatography on silica gel using a mixture of dichloromethane/ethanol (100/1) as the eluent. Yield: 28% (300 mg). MALDI-TOF-MS (DHB) m/z: 930.301 [M] +; calculated for C$_{48}$-H$_{48}$N$_8$S$_4$Zn: 930.588. FT-IR (ν, cm^{-1}) 3059, 2953, 1592, 1565, 1462, 1430, 1365, 1330, 1311, 1222, 1163, 1103, 1041, 946, 900, 881, 792, 757, 735, 679. ^{1}H NMR (500 MHz, DMSO-d_6) δ, ppm: 8.97–8.91 (m, 3H), 8.66–8.60 (m, 2 H), 8.06–7.59 (m, 8 H), 3.38–3.16 (m, 8 H), 2.23 (m, 4 H), 1.31 (m, 24 H). UV-vis (THF): λ_{max}, nm (logε): 710 (5.3), 641 (4.6), 340 (4.9).

2.1.4. Synthesis of the random copolymer poly(OEGMA$_{300}$-r-AEMA) (RCP). 10.55 mg (0.038 mmol) of 4-cyanopentanoic acid dithiobenzoate (CPADB) and 1.29 mg (0.0077 mmol) of AIBN, 1.83 mL (6.4 mmol) of OEGMA$_{300}$, 0.31 mL (1.6 mmol) of AEMAa and 3.37 mL of dioxane were added in this order. The system was sealed with a rubber septum and the mixture was then left to degas under inert gas for 15 minutes. After that time, the reaction mixture was maintained at 70 °C, under nitrogen positive pressure and under continuous magnetic stirring for 17 hours. M_n (kDa)= 99.6, PDI= 1.04, dn/dc = 0.185. AEMA content (mol%) = 20. ^{1}H NMR (400 MHz, CDCl$_3$) δ, ppm: 4.37 (m, CCO$_2$C$\underline{H}_2$CH$_2$CO$_2$CH$_2$), 4.18–4.11 (m, 2H, CCO$_2$CH$_2$C$\underline{H}_2$CO$_2$), 3.83–3.58 (m, CH$_2$OC$\underline{H}_2$CH$_2$), 3.41 (s, OC$\underline{H}_3$), 2.33 (s, CH$_2$COC$\underline{H}_3$), 1.81 (m, CCH$_2$), 1.04 (m, CCH$_3$), 0.87 (m, CCH$_3$).

2.1.5. Synthesis of the block copolymer poly(OEGMA$_{300}$)-b-poly(AEMA) (BCP). 29.25 mg (0.105 mmol) of CPADB and 3.45 mg (0.021 mmol) of AIBN were dissolved in 1.5 mL of anhydrous 1,4-dioxane. Then, 0.6 mL (3.144 mmol) of AEMA was added and the resulting mixture was left degassing purging nitrogen for 20 minutes. After this time, the solution was left stirring under nitrogen positive pressure and at 70 °C for 5 hours. Then, the reaction was quenched by freezing the mixture at -78 °C. 1 mL (0.014 mmol of macro-CTA) of the crude, 6 mL (21 mmol) of OEGMA$_{300}$, 2.3 mg (0.014 mmol) of

AIBN and 18 mL of 1,4-dioxane were degassed purging nitrogen for 20 minutes, then left stirring at 70 °C under positive nitrogen pressure for 17 hours. After this time, the reaction was quenched by cooling the mixture at −78 °C. The polymer was precipitated in a large excess of *n*-hexane (×40) for three consecutive times and dried under dynamic vacuum. M_n (kDa) = 71.8, PDI = 1.02, dn/dc = 0.185. AEMA content (mol%) = 14. ^{1}H NMR (400 MHz, CDCl$_3$) δ, ppm: 4.37 (m, CCO$_2$C$\underline{H}_2$CH$_2$-CO$_2$CH$_2$), 4.18–4.10 (m, 2H, CCO$_2$CH$_2$C$\underline{H}_2$CO$_2$), 3.77–3.57 (m, CH$_2$OC$\underline{H}_2$CH$_2$), 3.40 (s, OC$\underline{H}_3$), 2.32 (s, CH$_2$COC$\underline{H}_3$), 1.87 (m, CC$\underline{H}_2$), 1.04 (m, CC$\underline{H}_3$), 0.87 (m, CC$\underline{H}_3$).

2.1.6. Characterization of RCP and BCP. Molecular structure and copolymer composition were investigated *via* ^{1}H NMR spectroscopy, using a Bruker spectrometer operating at 400 MHz. AEMA content, expressed as %AEMA (mol%) was calculated according to eqn (1):

$$\%\text{AEMA(mol\%)} = \frac{S^{\text{AEMA}}_{\text{COCH}_3}}{S^{\text{AEMA}}_{\text{COCH}_3} + S^{\text{OEGMA}}_{\text{OCH}_3}} \times 100 \qquad (1)$$

where $S^{\text{AEMA}}_{\text{COCH}_3}$ is the signal intensity of the methylic protons of AEMA functional groups (δ: 2.3 ppm) and $S^{\text{OEGMA}}_{\text{OCH}_3}$ is the signal intensity of methoxylic protons of OEGMA moieties (δ: 3.4 ppm), both integrated taking $S^{\text{OEGMA}}_{\text{OCH}_3}$ as internal standard.

Number-average molecular weight (M_n) and dispersity ($Đ$) were determined *via* size exclusion chromatography/multi-angle light scattering (SEC/MALS) measurements, which were performed at 30 °C on an Agilent 1200 system equipped with PLgel 5 μm Guard and PLgel 5 μm MIXED-C columns and triple detection: a differential refractive index (dRI) detector (Optilab Rex, Wyatt), a multi-angle laser light scattering (MALS) detector (MiniDawn Treos, Wyatt), and a viscosimetric (VIS) detector (ViscoStar-II, Wyatt). THF was used as eluent at a flow rate of 1 mL min^{-1}.

The topology of **RCP** and **BCP** in water was determined from small-angle X-ray scattering (SAXS) measurements on polymer solutions at a fixed polymer concentration of 1 mg mL^{-1}. SAXS experiments were conducted on a Rigaku 3-pinhole PSAXS-L equipment operating at 45 kV and 0.88 mA. The MicroMax-002+ X-Ray Generator System is composed by a microfocus sealed tube source module and an integrated X-Ray generator unit which produces CuKα transition photons of wavelength λ = 1.54 Å. The radius of gyration (R_g) and size scaling exponent (ν) of **RCP** were determined through fits of the experimental data to a generalized Gaussian coil[29] function. For **BCP**, analysis of the SAXS data in terms of the Dozier[30] star model provided R_g and the average number of arms, f. In both cases the SASfit program was used.[31]

UV-vis measurements of **RCP** and **BCP** were carried out in water at 25 °C in an Agilent 8453A apparatus with Peltier thermostatic cell holder, T-controller 89090A.

2.1.7. General procedure for the encapsulation of Pc2 into RCP or BCP to give SCNP-Pc2$_x$ and SLA-Pc2$_x$, respectively. A stock solution of **Pc2** (0.25 mg mL^{-1}) was prepared by dissolving 1 mg (1.1 μmol) of **Pc2** in 4 mL of THF. 10 mg of **RCP** or **BCP** were dissolved in 1 mL of THF and **Pc2** stock

solution was added (186 μL or 447 μL). The resulting solution was left stirring for 48 hours until complete evaporation of the THF and the formation of a thin film. After this time, 10 mL of deionized water was added, and the resulting mixture was left stirring at room temperature for 3 days. **Pc2** concentration is therefore either 5 or 12 μM, and the respective nanoparticles are denoted as **SCNP-Pc2$_x$** or **SLA-Pc2$_x$** (x = 5 or 12).

2.1.8. Characterization of SCNP-Pc2$_x$ and SLA-Pc2$_x$. SCNP-Pc2$_x$ and SLA-Pc2$_x$ were characterized by SAXS and UV-vis, following the same procedures used for **RCP** and **BCP**, respectively.

2.2. Optical measurements

UV-visible electronic absorption spectrum was recorded on a Shimadzu 2001 UV spectrophotometer.

Fluorescence quantum yield of **Pc2** was determined by the comparative method according to the equation:

$$\Phi_F = \Phi_{F_{(\text{std})}} \times \frac{F.A_{(\text{Std})}.n^2}{F_{(\text{Std})}.A.n^2_{(\text{Std})}}$$

where F and F_{Std} are the areas under the emission curves for the sample and standard, respectively. A and A_{Std} are the absorbance at the excitation wavelength for the sample and standard, n is the refractive index of the solvents for the sample and reference. Unsubstituted **ZnPc** in DMSO was used as a standard ($\Phi F_{(\text{Std})}$ = 0.20) and sample and standard were excited (at λ= 640 nm) at the same wavelength in DMSO.

Singlet oxygen quantum yield of **Pc2** was obtained in DMSO solution (in air, no oxygen bubbled) by indirect method with zinc phthalocyanines (**ZnPc**) as a reference and 1,3-diphenylisobenzo-furan (DPBF) as a chemical quencher for singlet oxygen, using the fallowing equation:

$$\Phi_\Delta = \Phi_\Delta^{\text{Std}} \frac{R \cdot I_{\text{abs}}^{\text{Std}}}{R^{\text{Std}} \cdot I_{\text{abs}}}$$

where Φ_Δ^{Std} is the singlet oxygen quantum yield for the standard **ZnPc** (Φ_Δ = 0.67 in DMSO). R and R^{Std} are the DPBF photobleaching rates in the presence of **Pc2**, and the standard, respectively. I_{abs} and $I_{\text{abs}}^{\text{Std}}$ are the rates of light absorption by **Pc2** and standard, respectively. Mixture of phthalocyanine (∼6 μM, absorption ∼1.2 at 717 nm) and DPBF (∼30 μM, absorption ∼0.8 in 417 nm) was irradiated in the Q band region in 10 cycles of 5 s each one. DPBF degradation was monitored at 417 nm and the Φ_Δ value was determined using the set up described above.[32,33]

2.3. Biology

2.3.1. Materials. Human breast cancer cells (MCF-7) were purchased from American Type Culture Collection (ATCC), Dul-becco's modified Eagle's Medium (DMEM/F12), fetal bovine serum (FBS), and penicillin/streptomycin were purchased from Gibco Life Technology, 3-(4,5-dimethylthiazol-2-yl)-2,5-diphenyltetrazolium bromide (MTT) was purchased from Alfa Aesar (Thermofisher).

2.3.2. Cell culture. MCF-7 cells were maintained in DMEM/F12 supplemented with 10% FBS and 1% penicillin/streptomycin. Cells grew at 37 °C, in humidified atmosphere and under 5% CO$_2$.

2.3.3. Cytotoxicity studies. MCF-7 cells were seeded in a plastic multi-well (96) plate. The day after seeding, cells were incubated with increasing doses of nanoparticles (from 0 to 200 μg mL^{-1}) for 72 h. The viability of the cells incubated with nanoparticles was evaluated using MTT assay. For this, cells were incubated for 4 h with 0.5 mg mL^{-1} of MTT in media. The MTT/media solution was then removed, and the precipitated formazan crystals were dissolved in 150 μL of an equal volume solution of ethanol/DMSO. After 30 min, the optical density (OD) of samples was read at 540 nm using microplate reader. The OD values are directly correlated with the number of living cells in well. Cell viability was calculated as % viability = OD of treated cell/OD of vehicle control × 100.

2.3.4. PDT experiments. For continuous excitation (633, 650 or 740 nm), MCF-7 cells were seeded in a plastic multi-well (96) plate. The day after, cells were incubated with 100 μg mL^{-1} of **SCNP-Pc2$_x$** or **SLA-Pc2$_x$** for 24 h. After the incubation time, cells were exposed or not to light source at 633, 650 or 740 nm. The excitation at 633 nm (4.96 J cm^{-2}) was performed with an EVOS 5000 microscope using Cy5 EVOS LED light cube during 1 min, 64,9 mW at magnification 4×. The excitation at 650 nm (39 J.cm^{-2}) was performed with a portable laser during 20 min. The excitation at 740 nm (11.25 J m^{-2}) was performed with a LED spotlight from EvoluChem™ for 10 min. For pulsed laser excitation (800 nm), MCF-7 cells were incubated in a multi-well (384) plate with glass bottom. The day after, cells were incubated with 100 μg mL^{-1} of **SCNP-Pc2$_x$** or **SLA-Pc2$_x$** for 24 h, and then submitted or not to laser irradiation with a confocal Carl Zeiss two-photon microscope at 800 nm and maximum laser power (3 W input, 1100 mW output at lens). The laser beam was focused by a microscope objective lens (Carl Zeiss 10-fold magnification/objective 0.3 EC Plan-Neofluar) and irradiations were performed by 3 scans of 1.5 s each. Two days after irradiation, the phototoxicity effect of nanoparticles was assessed using MTT assay as previously described. Cells treated with the vehicle blank nanocarriers (**RCP** and **BCP**) were considered as a control.

2.3.5. Statistical analysis. Student's *t*-test was performed to compare paired groups of data. A *p* value < 0.05 was considered as statistically significant.

3. Results and discussion

3.1. Molecular design and synthesis of *iso*-butylthio non-peripherally tetrasubstituted Zn phthalocyanine (Pc2)

The photo-properties of phthalocyanines can be modulated by their substitution pattern.[34] The presence of *S*-alkyl substituents shifts their maximum absorption towards the red, as well as non-peripheral substitution. Bulky substituents are known to limit aggregation. Isobutyl moieties were selected to be introduced *via* thioether functions in one non-peripheral position of each of the four isoindole subunits of a Zn phthalocyanine. As shown in Scheme 1, the synthesis was readily achieved in two steps. First, phthalonitrile **1** was prepared by the reaction between isobutylthiol and 3-nitrophthalonitrile, in 80% yield. The corresponding phthalocyanine **Pc2** was obtained by reacting
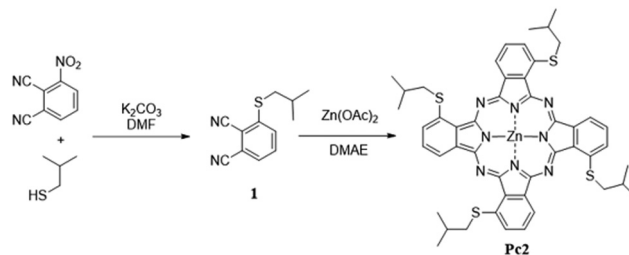
Scheme 1 Synthesis of phthalocyanine **Pc2** (only one of the existing regioisomers is shown).

phthalonitrile **1** in presence of Zn(OAc)$_2$, yielding the desired phthalocyanine in 28% yield and in rather large scale (300 mg). All analyses confirmed the proposed structure.

3.2. Photo-properties of Pc2

UV-vis spectra of **Pc2** have been recorded in THF, DMSO and chloroform at 10 micromolar, conditions for which **Pc2** is not aggregated. DMSO has been selected as the solvent for the next measurements to use the unsubstituted **ZnPc** as the standard, as all necessary reference data are available.[33] The maximum of the Q band is located at 717 nm, reflecting the bathochromic shift effect expected from both the non-peripheral and the alkylthio substitution (Fig. 1A), compared to unsubstituted phthalocyanine that absorbs at 675 nm in DMSO[33] corresponding to a substantial bathochromic shift of more than 40 nm. The fluorescence spectrum recorded in DMSO showed the expected shape and small Stokes shift. The fluorescence quantum yield of **Pc2** in DMSO was determined to be 0.07, in line with its high oxygen generation quantum yield ($\Phi_\Delta = 0.78$).

All the photo-properties of **Pc2** in DMSO are summarized in Table 1. All these collected data confirm the relevance of using **Pc2** for anti-cancer PDT, both for its strong absorption at far-red wavelength and its high ability to generate singlet oxygen. The fluorescence quantum yield of **Pc2** is lower than those of **ZnPc**, while its SO quantum yield is higher. This is due to the presence of the sulfur atom on the phthalocyanine macrocycle, which is known to exert a heavy atom effect increasing the intersystem crossing.[35]

3.3. Synthesis of RCP and BCP nanocarriers and encapsulation of Pc2.

3.3.1 Synthesis of RCP and BCP. Two kind of nanocarriers comprising hydrophilic oligo(ethylene glycol) monomethyl ether methacrylate (OEGMA$_{300}$) and hydrophobic (2-acetoacetoxy)ethyl methacrylate (AEMA) repeat units were investigated: a random copolymer (**RCP**) and a block copolymer (**BCP**) (Scheme 2). Due to their intrinsic amphiphilic nature, both can self-assemble in aqueous media in ultra-dilute conditions, yielding self-assembled structures whose topology can vary with the architecture of the starting copolymer. Both nanocarriers were synthesized *via* RAFT copolymerization of the commercially available monomers, using 4-cyanopentanoic acid dithiobenzoate (CPADB) as chain transfer agent (Scheme 2). After purification *via* precipitation in *n*-hexane and drying under dynamic vacuum, the isolated **RCP** and **BCP** were characterized by means of SEC/MALS and quantitative ^{1}H NMR
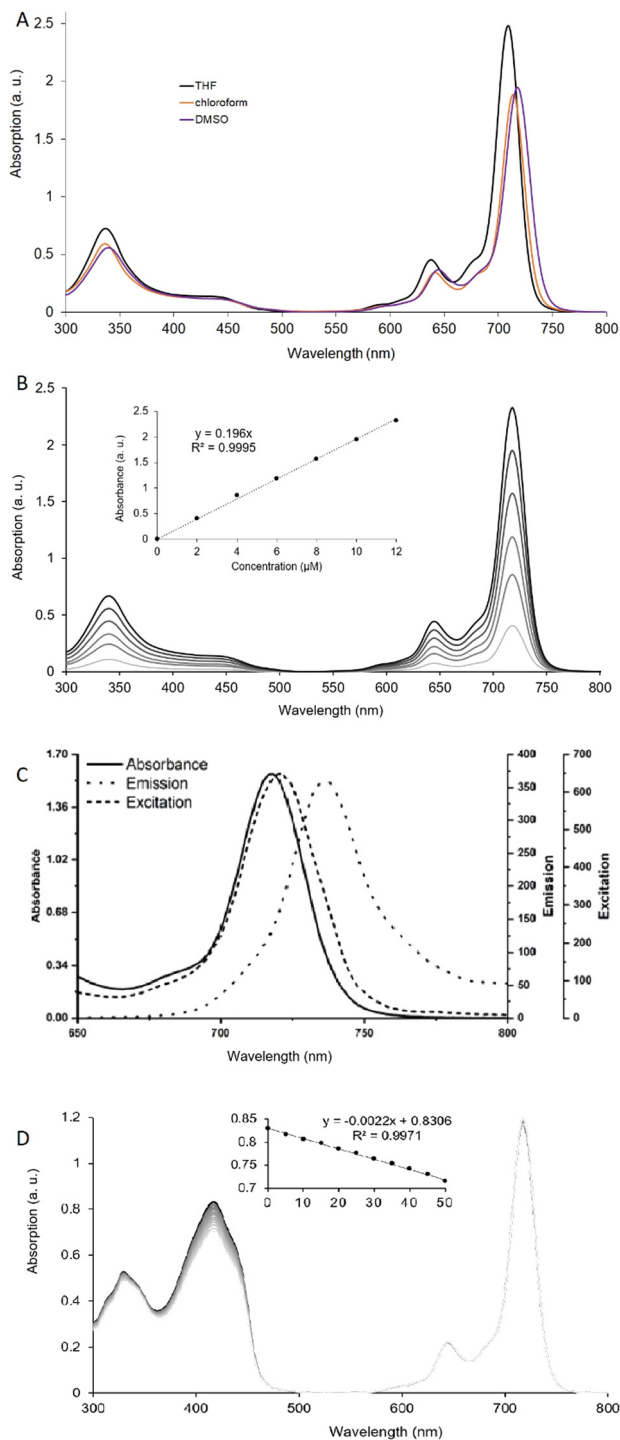
Fig. 1 (A) Superimposed UV–vis spectra of **Pc2** in chloroform, DMSO and THF (10 μM). (B) UV–vis absorption spectra of **Pc2** in DMSO (2–12 μM). Inset: Absorption *vs.* concentration. (C) Absorbance, emission (irradiation: 640 nm), and excitation spectra of **Pc2** in DMSO. (D) Determination of singlet oxygen quantum yield of **Pc2** in DMSO (6 μM). Inset: Plot of DPBF absorbance at 417 nm *vs.* time.

spectroscopy for the determination of M_n, $Đ$ and copolymer composition (see Table 2).

The self-assembled blank nanoparticles (without phthalocyanine) **SCNP-Pc2$_0$** (formed by **RCP**) and **SLA-Pc2$_0$** (formed by

Table 1 Photo-properties of **Pc2** in DMSO

λ_{max} (nm)	$\log \varepsilon$	λ_{Em} (nm)	λ_{Exc} (nm)	$\Delta\lambda_{Stokes}$ (nm)	Φ_F	Φ_Δ
717	5.29	736	720	16	0.07	0.78
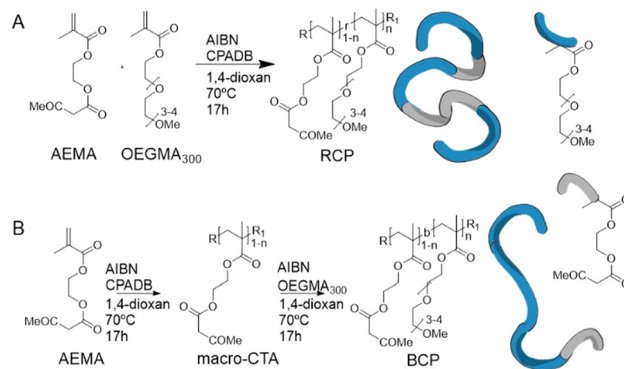
Scheme 2 (A) Pictorial representation of the copolymerization reaction of the hydrophobic monomer AEMA (depicted in grey) and the hydrophilic monomer OEGMA$_{300}$ (depicted in blue) to give **RCP**. (B) Reaction scheme for the synthesis of the amphiphilic block copolymer **BCP**.

BCP) at high dilution ([polymer] = 1 mg mL^{-1}) in water were investigated by SAXS measurements. As illustrated in Fig. 2a, **RCP** in water at high dilution was found to form **SCNP-Pc2$_0$** as determined by SAXS experiments. Due to the impossibility to perform SAXS experiments in the conditions that mimic the cell culture, SAXS experiments were performed in water in dilute conditions. Previous works by our group have confirmed the self-assembly of these amphiphilic random copolymers into globular like core–shell single-chain nanoparticles at a concentration well above the overlap concentration.[36,37] Concerning the use of the generalized Gaussian coil model to fit the SAXS data of **RCP** it is well-established in the literature.[25] The average radius of gyration (R_g) of the **SCNPs** was $R_{g,water}$ = 10.4 nm (a value smaller than that found in THF solvent, $R_{g,THF}$ = 14.4 nm). The **SCNPs** were found to have a sparse conformation as revealed by the high value of the size scaling exponent (ν = 0.59). We attribute the open conformation of the **SCNPs** to the relatively small amount of hydrophobic AEMA units in **RCP**. On the other hand, **BCP** at high dilution in water self-assembled into star-like assemblies (**SLA-Pc2$_0$**) of $R_{g,water}$ = 10.0 nm having (on average) 2 arms each one (*i.e.*, forming dimers). As we will see below, the number of arms per star increases upon encapsulation of **Pc2**. Concerning the SAXS data of **BCP**, the validity of the Dozier Star model to fit the SAXS data of star-like polymers is supported both by simulations and experimental

Table 2 Number average molecular weight (M_n), dispersity ($Đ$) and copolymer composition of **RCP** and **BCP**

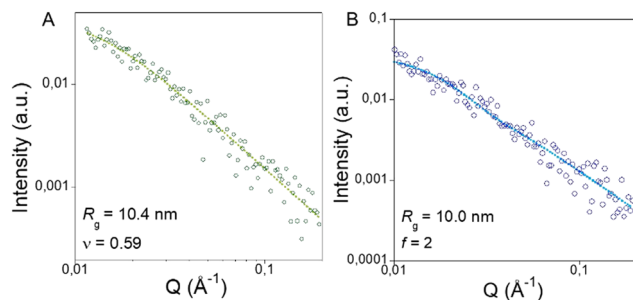| Copolymer	M_n/kDa	$Đ$	AEMA/mol%	OEGMA$_{300}$/mol%
RCP	99.6	1.04	20	80
BCP	71.8	1.02	14	86

Fig. 2 (A) SAXS results revealing the form factor of **SCNP-Pc2$_0$** in water. Line is a fit of a generalized Gaussian coil function, yielding the values of the R_g and ν parameters. (B) SAXS results revealing the form factor of **SLA-Pc2$_0$** in water. Line is a fit of the Dozier star model, yielding the values of the R_g and f parameters.

results.[38] It is worth noting that the UV-vis spectra of **SCNP-Pc2$_0$** (formed by **RCP**) and **SLA-Pc2$_0$** (formed by **BCP**) showed no absorption bands in the 600–700 nm wavelength region (Fig. S8, ESI†).

3.3.2. Encapsulation of Pc2. Both **Pc2**-containing **SCNP-Pc2$_x$** and **SLA-Pc2$_x$** were prepared using the same encapsulation procedure by starting with **RCP** or **BCP**, respectively. The experimental conditions for the encapsulation of **Pc2** were first optimized exploring different polymer concentrations in solution. As explained above, we observed that the optimal working range for self-folding into **SCNPs** is from 0.1 mg mL^{-1} to 5 mg mL^{-1} for **RCP** and that **BCP** dimers start to form from a concentration of 1 mg mL^{-1}. Regarding the concentration of loadable **Pc2**, we looked for the highest achievable quantity of **Pc2** to be compatible with the formation of **SCNPs** when using the less possible amount of **RCP** precursor, ensuring the highest possible **Pc2**/polymer ratio. This latter is a less flexible system, when compared to multi-chain aggregates, in terms of hydrophilic/hydrophobic interactions changes in the media, and constituted indeed our limiting factor for the optimization of the encapsulation procedure. We attempted the encapsulation fixing the photosensitizer concentration at 20 μM, which resulted in irreversible aggregation when using **RCP** as nanocarrier. For this reason, we progressively lowered the photosensitizer loading up to 12 μM, which finally resulted to be the maximum working **Pc2** concentration. In addition, we selected the polymer concentration of 1 mg mL^{-1} as it is the lowest nanocarrier amount needed in solution to efficiently encapsulate the photosensitizer at its maximum achievable loading. To explore the effect of the loading amount, two different concentrations of **Pc2** (x = 5 μM or 12 μM) were used for both copolymers, yielding for both the nanoparticles architectures (**SCNPs** or **SLAs**) the title phthalocyanine photosensitizer-encapsulated nanocarriers at the loading regimes of 4.7 μg per mg of polymer for **SCNP-Pc2$_5$** and **SLA-Pc2$_5$** and 11.2 μg per mg of polymer for **SCNP-Pc2$_{12}$** and **SLA-Pc2$_{12}$**.

3.3.3. Characterization of SCNP-Pc2$_x$. SAXS experiments confirmed the successful formation of **SCNP-Pc2$_5$** and **SCNPs-Pc2$_{12}$**, as illustrated in Fig. 3. Hence, a small reduction in size and in scaling exponent was observed upon increasing the amount of encapsulated **Pc2**. This may be because **Pc2** is
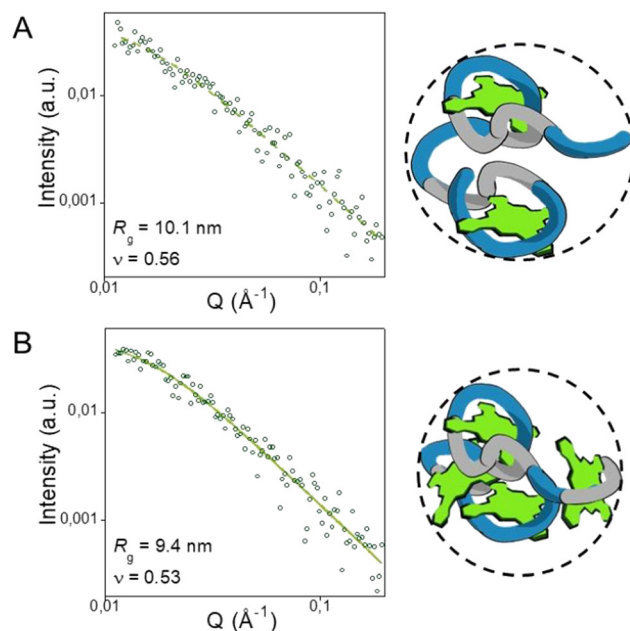

Fig. 3 SAXS results and respective depictions of the morphologies revealed, with form factor in water of **SCNP-Pc2$_5$** (A) and **SCNP-Pc2$_{12}$** (B), Values of R_g and ν were obtained through fits of a generalized Gaussian coil function (continuous lines) to the experimental data.

hydrophobic, so to encapsulate it the polymeric chain wraps the **Pc2** complex, and this generates a compaction of the chain accompanied by a reduction in size. Table 3 shows the values of the fitting parameters for SAXS curves of **SCNP-Pc2$_0$** (blank nanoparticles without phthalocyanine), **SCNP-Pc2$_5$** and **SCNP-Pc2$_{12}$** in water, applying a generalized Gaussian coil function.

UV-vis spectra of **SCNPs-Pc2$_5$** and **SCNPs-Pc2$_{12}$** in water revealed an intense absorption in the 600–700 nm wavelength region (Fig. 4). The splitted shape of the Q band indicates that **Pc2** is aggregated inside the nanocarrier.

3.3.4. Characterization of SLA-Pc2$_x$. SAXS results of **SLA-Pc2$_5$** and **SLA-Pc2$_{12}$** are illustrated in Fig. 5. Both nanocarriers in water at high dilution form star-like assemblies (**SLAs**) with a larger number of arms and slightly larger size than **BCP** (f = 2 arms, $R_{g,water}$ = 10.0 nm). Analysis of the SAXS form factor of **SLA-Pc2$_5$** in terms of the Dozier star model provided f = 4 arms with $R_{g,water}$ = 10.1 nm, whereas **SLA-Pc2$_{12}$** displayed f = 8 arms and $R_{g,water}$ = 10.2 nm. Table 4 shows the values of the fitting parameters for SAXS curves of **BCP**, **SLA-Pc2$_5$** and **SLA-Pc2$_{12}$** in water, applying the Dozier star model.

The characteristic UV-vis absorption bands of **Pc2** encapsulated into **SLA-Pc2$_5$** and **SLA-Pc2$_{12}$** are reported in Fig. 6 and show the aggregated state of the phthalocyanine inside the nanoparticles.

3.4. *In vitro* photodynamic efficiency of SCNP-Pc2$_x$ and SLA-Pc2$_x$

The biological activity of the **SCNP-Pc2$_x$** and **SLA-Pc2$_x$** was studied on MCF-7 human breast cancer cells. Blank nanocarriers without **Pc2** (**RCP** and **BCP**) were also tested to assess their own biocompatibility.

Table 3 Fitting parameters values for SAXS curves of **SCNP-Pc2$_0$**, **SCNP-Pc2$_5$** and **SCNP-Pc2$_{12}$** in water, applying a generalized Gaussian coil function

	SCNP-Pc2$_0$	SCNP-Pc2$_5$	SCNP-Pc2$_{12}$
R_g (nm)	10.4	10.1	9.4
ν	0.60	0.56	0.53
I_0	0.048	0.053	0.053

Table 4 Fitting parameters values for SAXS curves of **SLA-Pc2$_0$**, **SLA-Pc2$_5$** and **SLA-Pc2$_{12}$** in water, applying Dozier star model

	SLA-Pc2$_0$	SLA-Pc2$_5$	SLA-Pc2$_{12}$
R_g (nm)	10.0	10.1	10.2
f	2	4	8
ν	0.60	0.60	0.60
I_0	0.040	0.052	0.068
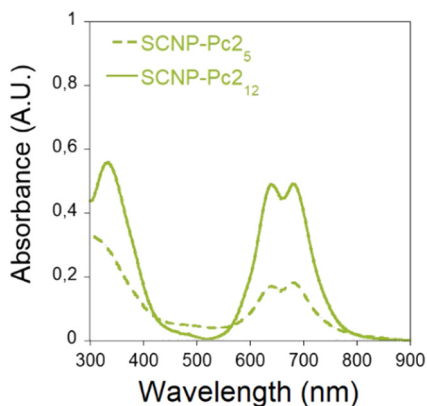
Fig. 4 UV-vis spectra of **SCNP-Pc2$_5$** and **SCNP-Pc2$_{12}$** in water (1 mg mL^{-1}).
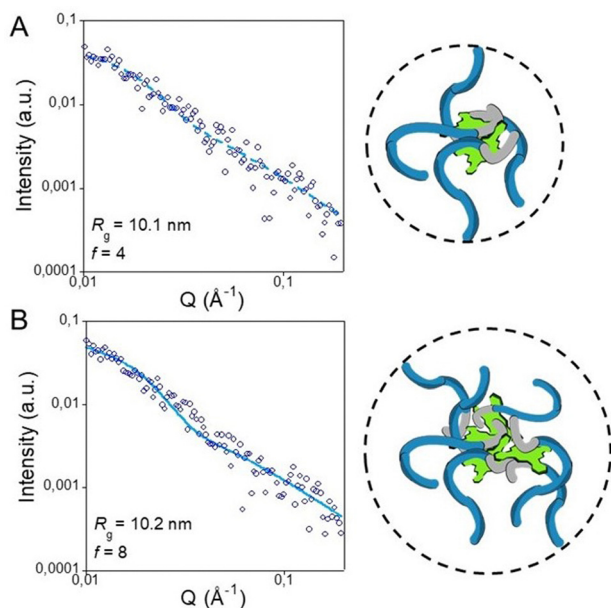

Fig. 5 SAXS results and respective depictions of the morphologies revealed, with form factor in water of **SLA-Pc2$_5$** (A) and **SLA-Pc2$_{12}$** (B). Values of R_g and arm number (f) were obtained through fits of the Dozier star model to the experimental data (continuous lines).

3.4.1. Cytotoxicity. First, the cytotoxic effect in the dark was analyzed by incubating the cells during 72 h with increasing concentrations of **SCNP-Pc2$_x$** or **SLA-Pc2$_x$** (from 1 to 200 μg mL^{-1}). The corresponding concentrations of **Pc2** for

each nanocarrier were calculated (in μg mL^{-1} and in μM) and reported in the Table S1 (ESI†). The cells were submitted to a MTT colorimetric assay, and the quantification of living cells was performed (Fig. 7A). All the nanocarriers, either empty or phthalocyanine-loaded, induced no more than 50% cell death, even at the highest concentrations (200 μg mL^{-1}). This observation let us to fix a concentration of 100 μg mL^{-1} for PDT experiments.

3.4.2. Photodynamic therapy. Next, to evaluate the photodynamic potential of the **Pc2**-loaded nanocarriers, MCF-7 cells were incubated with 100 μg mL^{-1} of distinct nanocarriers loaded with 5 or 12 μM of phthalocyanine (*i.e.*, **SCNP-Pc2$_5$**, **SCNP-Pc2$_{12}$**, **SLA-Pc2$_5$** and **SLA-Pc2$_{12}$**) for 24 h and exposed or not to laser irradiation at various wavelengths (633, 650 and 740 nm). These wavelengths correspond to the absorption range of **Pc2** when encapsulated into the nanocarriers, as its Q band is enlarged due to their aggregated state inside the nanocarrier. Living cell percentage quantification was performed 2 days after irradiation (Fig. 7B). **SCNP-Pc2$_5$** and **SCNP-Pc2$_{12}$** did not exhibit significant phototoxicity, while **SLA-Pc2$_5$** and **SLA-Pc2$_{12}$** resulted in significant efficiency. **SLA-Pc2$_{12}$** excited at 650 nm and **SLA-Pc2$_5$** excited at 740 nm gave the best results with 47% and 73% cell death, respectively. When comparing the absorption spectra of **SCNP-Pc2$_5$** with **SCNP-Pc2$_{12}$** (as well as for **SLA-Pc2$_5$** *vs.* **SLA-Pc2$_{12}$**), no significant difference was observed. For this reason, we ascribed the augmented PDT-effect in **SLA-Pc2$_x$** to the more flexible structure and peculiar topology of these **BCP**-based nanocarriers that accommodate **Pc2** in a manner favoring likely better ROS generation. In parallel, we have verified the cytotoxicity and PDT potential of free **Pc2**. For this, MCF-7 cells were incubated
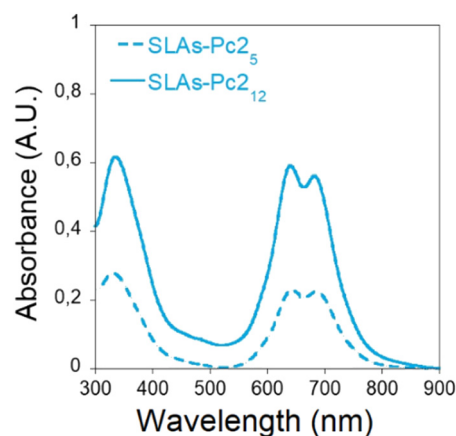

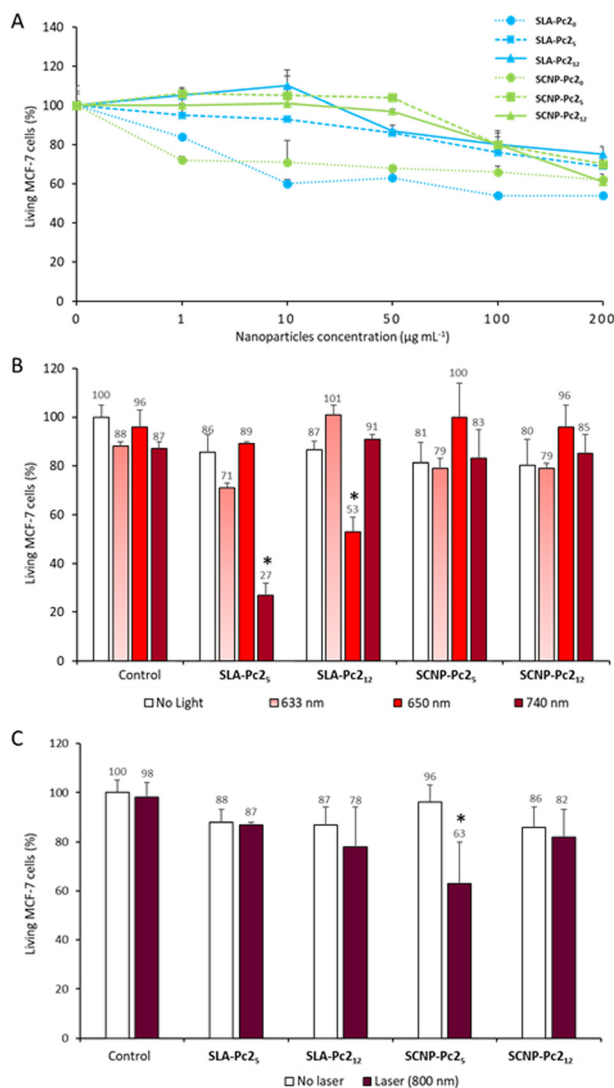**Fig. 6** UV-vis spectra of **SLA-Pc2$_5$** and **SLA-Pc2$_{12}$** in water (1 mg mL^{-1}).

Fig. 7 (A) Cell viability study of MCF-7 cells incubated 72 h with increasing concentrations (from 1 to 200 μg mL^{-1}) of **SCNP-Pc2$_5$**, **SCNP-Pc2$_{12}$**, **SLA-Pc2$_5$** and **SLA-Pc2$_{12}$**. (B) PDT effect of **SCNP-Pc2$_5$**, **SCNP-Pc2$_{12}$**, **SLA-Pc2$_5$** and **SLA-Pc2$_{12}$** (100 μg mL^{-1}) incubated 24 h with MCF-7 cells and excited at 633, 650 and 740 nm. (C) PDT effect of **SCNP-Pc2$_5$**, **SCNP-Pc2$_{12}$**, **SLA-Pc2$_5$** and **SLA-Pc2$_{12}$** (100 μg mL^{-1}) incubated 24 h with MCF-7 cells and excited at 800 nm, with a pulsed laser. Data are means ± SEM; $n = 3$. * $p < 0.05$, significantly different from "No laser".

with increasing concentrations of **Pc2** and didn't show any toxicity for these concentrations (Fig. S11A, ESI†). Cells were then incubated with 0.5 or 1.2 μg mL^{-1} of **Pc2** (corresponding to 100 μg mL^{-1} of **SCNP-Pc2$_5$**, **SCNP-Pc2$_{12}$**, **SLA-Pc2$_5$**, **SLA-Pc2$_{12}$**) and submitted to 633 nm, 650 nm and 740 nm excitation. Data demonstrated an absence of PDT potential without encapsulation (Fig. S11B, ESI†). This result highlights the necessity of **Pc2** encapsulation for a biological application. In addition, reactive oxygen species (ROS) production was detected under light excitation at 650 nm when cells were incubated with **SLA-Pc2$_{12}$** but not with free **Pc2** (1.2 μg mL^{-1}) (Fig. S12, ESI†).

It is well-known that aggregated photosensitizers - including phthalocyanines - have a self-quenched inter-system crossing pathway, negatively affecting their photodynamic efficiency when excited classically by monophotonic light source. On the other hand, aggregated phthalocyanines, as in the case of phthalocyanine-based organosilica nanoparticles previously reported by some of us,[20,21] may exhibit good photo-killing effect when excited by pulsed laser at NIR wavelengths. The photodynamic efficiency of **SCNP-Pc2$_5$**, **SCNP-Pc2$_{12}$**, **SLA-Pc2$_5$** and **SLA-Pc2$_{12}$**, still at 100 μg mL^{-1}, was therefore studied with a pulsed laser irradiating at 800 nm (Fig. 7C) in the first NIR phototherapeutic window. Under such conditions, **SCNP-Pc2$_5$** resulted to be the only nanoparticle to exhibit significant photo-killing ability. Indeed, we can observe 36% cell death when cells, previously incubated with **SCNP-Pc2$_5$**, were submitted to 800 nm excitation wavelength using a pulsed laser, from Chameleon lamp of a confocal microscope (3 successive scans of 1.5 s). The comparison between **SCNP-Pc2$_5$** (4.7 μg per mg of polymer) and its higher-**Pc2**-loaded analogue **SCNP-Pc2$_{12}$** (11.2 μg per mg of polymer) shows that here also the loading is important, as too much phthalocyanine in the **SCNP** carrier prevents a good efficency. Overall, the different behavior of these phthalocyanine-loaded nanocarriers can be attributed to their different nanocarrier topology: self-folded single-chain nanoparticles (**SCNPs**) vs. star-like aggregates (**SLAs**), respectively.

4. Conclusions

Two different amphiphilic copolymers encapsulating **Pc2** within self-folded single-chain nanoparticles (**SCNPs**) and star-like aggregates (**SLAs**), have demonstrated their relevance as photosensitizer nanocarriers for PDT of cancer cells, under excitation in the infrared range with pulsed laser or in the visible range with continuous laser, respectively. In addition, free **Pc2** is not biologically active in these conditions. All together, these results demonstrate the interest and the novelty of these nanocarrier systems for the encapsulation and delivery of photosensitizers for PDT.

Author contributions

DA, MO, CN, ZŞ: data curation, investigation, formal analysis and manuscript writing. Üİ, EVS, AI, AA: data curation, supervision, formal analysis, methodology and manuscript writing. FD, JAP and MGB: supervision, conceptualization, resources, project administration and manuscript writing.

Data availability

The data supporting this article have been included as part of the ESI.†

Conflicts of interest

There are no conflicts to declare.

Notes and references

1 J. Kou, D. Dou and L. Yang, *Oncotarget*, 2017, **8**, 81591–81603.

2 D. Kessel, *J. Clin. Med.*, 2019, **8**(10), 1581.

3 C. Frochot and S. Mordon, *J. Porphyrins. Phthalocyanines*, 2019, **23**, 347–357.

4 M. Penetra, L. G. Arnaut and L. C. Gomes da Silva, *OncoImmunology*, 2023, **12**, 2226535.

5 R. Baskaran, J. Lee and S. G. Yang, *Biomater. Res.*, 2018, **22**, 25.

6 M. Wainwright, *Color. Technol.*, 2010, **126**, 115–126.

7 B. Pucelik, A. Sułek and J. M. Dąbrowski, *Coord. Chem. Rev.*, 2020, **416**, 213340.

8 P.-C. Lo, M. S. Rodríguez-Morgade, R. K. Pandey, D. K. P. Ng, T. Torres and F. Dumoulin, *Chem. Soc. Rev.*, 2020, **49**, 1041–1056.

9 Y. Zhang and J. F. Lovell, *Wiley Interdiscip. Rev.: Nanomed. Nanobiotechnol.*, 2017, **9**, e1420.

10 V. Almeida-Marrero, E. van de Winckel, E. Anaya-Plaza, T. Torres and A. de la Escosura, *Chem. Soc. Rev.*, 2018, **47**, 7369–7400.

11 X. Li, B.-D. Zheng, X.-H. Peng, S.-Z. Li, J.-W. Ying, Y. Zhao, J.-D. Huang and J. Yoon, *Coord. Chem. Rev.*, 2019, **379**, 147–160.

12 F. Dumoulin, M. Durmus, V. Ahsen and T. Nyokong, *Coord. Chem. Rev.*, 2010, **254**, 2792–2847.

13 G. Obaid, M. Broekgaarden, A.-L. Bulin, H.-C. Huang, J. Kuriakose, J. Liu and T. Hasan, *Nanoscale*, 2016, **8**, 12471–12503.

14 S. Wilhelm, A. J. Tavares, Q. Dai, S. Ohta, J. Audet, H. F. Dvorak and W. C. W. Chan, *Nat. Rev. Mater*, 2016, **1**, 16014.

15 W. G. Love, S. Duk, R. Biolo, G. Jori and P. W. Taylor, *Photochem. Photobiol.*, 1996, **63**, 656–661.

16 B. Pucelik, I. Gürol, V. Ahsen, F. Dumoulin and J. M. Dąbrowski, *Eur. J. Med. Chem.*, 2016, **124**, 284–298.

17 E. G. Pehlivan, Y. Ek, D. Topkaya, U. H. Tazebay and F. Dumoulin, *J. Porphyrins. Phthalocyanines*, 2019, **23**, 1587–1591.

18 L. V. Kiew, H. Y. Cheah, S. H. Voon, E. Gallon, J. Movellan, K. H. Ng, S. Alpugan, H. B. Lee, F. Dumoulin, M. J. Vicent and L. Y. Chung, *Nanomedicine*, 2017, **13**, 1447–1458.

19 H. Y. Cheah, E. Gallon, F. Dumoulin, S. Z. Hoe, N. Japundžić-Žigon, S. Glumac, H. B. Lee, P. Anand, L. Y. Chung, M. J. Vicent and L. V. Kiew, *Mol. Pharmaceutics*, 2018, **15**, 2594–2605.

20 G. Ekineker, C. Nguyen, S. Bayir, S. Dominguez-Gil, U. Isci, M. Daurat, A. Godefroy, L. Raehm, C. Charnay, E. Oliviero, V. Ahsen, M. Gary-Bobo, J.-O. Durand and F. Dumoulin, *Chem. Commun.*, 2019, **55**, 11619–11622.

21 C. Mauriello-Jimenez, M. Henry, D. Aggad, L. Raehm, C. Charnay, X. Cattoen, M. W. C. Man, S. Alpugan, V. Ahsen, D. K. Tarakcı, P. Maillard, M. Maynadier, M. Garcia, F. Dumoulin, M. Gary-Bobo, J.-L. Coll, V. Josserand and J.-O. Durand, *Nanoscale*, 2017, **9**, 16622–16626.

22 L. P. Gergely, Ç. Yüceel, Ü. İşci, F. S. Spadin, L. Schneider, B. Spingler, M. Frenz, F. Dumoulin and M. Vermathen, *Mol. Pharmaceutics*, 2023, **20**, 4165–4183.

23 A. Pia, P. Kröger and J. M. J. Paulusse, *J. Controlled. Release*, 2018, **286**, 326–347.

24 A. Pia, P. Kröger, N. M. Hamelmann, A. Juan, S. Lindhoud and J. M. J. Paulusse, *ACS Appl. Mater. Interfaces*, 2018, **10**, 30946–30951.

25 *Single-Chain Polymer Nanoparticles: Synthesis, Characterization, Simulations, and Applications*, ed. Pomposo, J. A., John Wiley & Sons, Weinheim, Germany, 2017.

26 Y. Liu, S. Pujals, P. J. M. Stals, T. Paulöhrl, S. I. Presolski, E. W. Meijer, L. Albertazzi and A. R. A. Palmans, *J. Am. Chem. Soc.*, 2018, **140**, 3423–3433.

27 J. Jeong, Y.-J. Lee, B. Kim, B. Kim, K.-S. Jung and H.-J. Paik, *Polym. Chem.*, 2015, **6**, 3392–3397.

28 W. W. Kramer and C. C. L. McCrory, *Chem. Sci.*, 2016, **7**, 2506–2515.

29 B. Hammouda, *Macromol. Theory Simul.*, 2012, **21**, 372–381.

30 W. D. Dozier, J. S. Huang and L. Fetters, *J. Macromol.*, 1991, **24**, 2810–2814.

31 I. Breßler, J. Kohlbrecher and A. F. Thünemann, *J. Appl. Crystallogr.*, 2015, **48**, 1587–1598.

32 S. Silva, P. M. Pereira, P. Silva, F. A. A. Paz, M. A. Faustino, J. A. Cavaleiro and J. P. Tomé, *Chem. Commun.*, 2012, **48**(30), 3608–3610.

33 M. Idowu and T. Nyokong, *J. Photochem. Photobiol., A*, 2007, **188**(2–3), 200–206.

34 S. Z. Topal, Ü. İşci, U. Kumru, D. Atilla, A. G. Gürek, C. Hirel, M. Durmuş, J.-B. Tommasino, D. Luneau, S. Berber, F. Dumoulin and V. Ahsen, *Dalton Trans.*, 2014, **43**, 6897–6908.

35 C. Farley, N. V. S. D. K. Bhupathiraju, B. J. John and C. M. Drain, *J. Phys. Chem. A*, 2016, **120**, 7451–7464.

36 A. Sanchez-Sanchez, A. Arbe, J. Kohlbrecher, J. Colmenero and J. A. Pomposo, *Macromol. Rapid Commun.*, 2015, **36**, 1592–1597.

37 B. Robles-Hernández, E. González, J. A. Pomposo, J. Colmenero and Á. Alegría, *Soft Matter*, 2020, **16**, 9738–9745.

38 C. N. Likas, *Soft Matter*, 2006, **2**, 478–498.

© 2025 The Author(s). Published by the Royal Society of Chemistry